A Versatile Chitosan-based Hydrogel Accelerates Infected Wound Healing *via* Bacterial Elimination, Antioxidation, Immunoregulation, and Angiogenesis

Ye Zhang, Sinan Chen, Xian Qin, Ai Guo, Kai Li, Lixue Chen, Weiwei Yi, Zhongliang Deng, Franklin R. Tay, Wenbo Geng*, Li Miao*, Yang Jiao*, Bailong Tao*

Y. Zhang, S Chen, A. Guo, K. Li, Prof. L. Chen, Prof. B. Tao

Laboratory Research Center, The First Affiliated Hospital of Chongqing Medical University, Chongqing 400016, PR China

E-mail: taobailong@hospital.cqmu.edu.cn

X. Qin

Women and Children's Hospital of Chongqing Medical University, Chongqing 401147, PR China

W. Yi

Department of Rehabilitation Medicine, The First Affiliated Hospital of Chongqing Medical University, Chongqing 400016, PR China

Prof. Z. Deng

Department of OrthopediCP, The Second Affiliated Hospital of Chongqing Medical University, Chongqing 400010, China

Prof. F. R. Tay,

The Graduate School, Augusta University, Augusta, GA 30912 USA.

Prof.W. Geng

WILEY-VCH

Chongqing Key Laboratory of Ophthalmology, The First Affiliated Hospital of Chongqing Medical University, Chongqing 400016, PR China

E-mail: 20191901690@cqu.edu.cn

Prof. L. Miao, Prof. Y. Jiao

Department of Stomatology, The Seventh Medical Center of PLA General Hospital, Beijing 100700, PR China.

E-mail: 615695111@qq.com, jiaoyang1989731@163.com

Drug-resistant bacterial infection of cutaneous wounds causes great harm to the human body. These infections are characterized by a microenvironment with recalcitrant bacterial infections, persistent oxidative stress, imbalance of immune regulation, and suboptimal angiogenesis. Treatment strategies available to date are incapable of handling the healing dynamics of infected wounds. A Schiff base and borate ester cross-linked hydrogel, based on phenylboronic acid-grafted chitosan (CS-PBA), dibenzaldehyde-grafted poly (ethylene glycol) (PEG-DA), and tannic acid (TA), is fabricated in the present study. Customized phenylboronic acid-modified zinc oxide nanoparticles (ZnO) are embedded in the hydrogel prior to gelation. The CPP@ZnO-P-TA hydrogel effectively eliminates methicillin-resistant *Staphylococcus aureus* (MRSA) due to the pH-responsive release of Zn^{2+} and TA. Killing is achieved via membrane damage, ATP reduction, leakage of intracellular components, and

hydrolysis of bacterial o-nitrophenyl-β-D-galactopyranoside. The CPP@ZnO-P-TA hydrogel is capable of scavenging reactive oxygen and nitrogen species, alleviating oxidative stress, and stimulating M2 polarization of macrophages. The released Zn^{2+} and TA also induce neovascularization via the PI3K/Akt pathway. The CPP@ZnO-P-TA hydrogel improves tissue regeneration *in vivo* by alleviating inflammatory responses, stimulating angiogenesis, and facilitating collagen deposition. These findings suggest that this versatile hydrogel possesses therapeutic potential for the treatment of MRSA-infected cutaneous wounds.

1. Introduction

Skin is the first line of defense for the human body against infections. It is vulnerable to damage by external hazards such as trauma, burns, surgery, or pathogenic bacterial infections[1]. Methicillin-resistant *Staphylococcus aureus* (MRSA) is a highly invasive Gram-positive pathogen. It is the primary etiological agent of cutaneous wound infections[2]. Rapid proliferation of MRSA results in the accumulation of substantial lactic acid in the infected wounds. This creates an acidic microenvironment (pH 5.5) that is significantly more acidic than the physiological environment (pH 7.4)[3]. Wound healing is a highly organized process that involves four distinct phases: hemostasis, inflammation, proliferation, and tissue remodeling[4]. Infected wounds are characterized by dysfunction of endothelial cells and fibroblasts, accumulation of inflammatory cells, and accumulation of reactive oxygen species

(ROS). These events eventually result in destruction of the extracellular matrix (ECM), over-expression of pro-inflammatory cytokines, and reduced angiogenesis[5]. Accelerated healing of infected cutaneous wounds is highly desirable for eradication of bacterial infection, scavenging of ROS, alleviation of inflammatory reactions, and stimulation of angiogenesis.

Eradication of bacterial infection improves healing of cutaneous wounds by ameliorating the harmful microenvironment of the infected wound tissues[6]. Local application of antibiotics is often used for the treatment of infected cutaneous wounds[7]. However, bacteria that survived this treatment regimen are prone to develop bacterial drug resistance. This poses a severe threat for public health management[8]. Consequently, there is an urgent need to develop a wound dressing with pH-responsive capacity, low toxicity, and antibiotics-free capacity. Apart from bacterial infections, another important property of infected wounds is their severe and long-term inflammatory responses[9]. Macrophages play a significant role in the tuning of inflammatory responses. These immune cells possess high plasticity and can be stimulated into different phenotypes. These phenotypes are generally classified as pro-inflammatory macrophages (M1 phenotype) and anti-inflammatory macrophages (M2 phenotype)[10]. During the early stages of wound healing, macrophages with the M1 phenotype amplify the inflammatory cascade *via* the production of high concentrations of pro-inflammatory cytokines, such as tumor necrosis factor-α (TNF-α), interleukinIL-1β (IL-

4

1β), and inducible nitric oxide synthase (iNOS) to resist invasive bacteria. During the late stages of wound healing, macrophages with the M2 phenotype participate in immunomodulation, stimulate neovascularization, and improve tissue remodeling through the secretion of growth factors such as transforming growth factor-β (TGF-β), vascular endothelial growth factor (VEGF), and platelet-derived growth factor (PDGF)[11]. Both M1 and M2 phenotype macrophages contribute to healing of infected wounds. However, persistent M1 macrophage polarization, and subsequently dysregulated balance of the M1/M2 phenotype, are responsible for the delay healing of cutaneous wounds. Timely M2 phenotype polarization causes the transition from inflammatory to remodeling stages and expedites wound healing.

Different types of wound dressings have been developed to facilitate wound healing. These dressings include electrospun nanofibers, membranes, porous foams, sponges, and hydrogels. They are capable of retaining wound moisture, and resisting bacterial invasion[12]. Considerable attention has been devoted lately to hydrogel dressings because of their intrinsic porous structure, high water retention capacity, ability to absorb excessive tissue exudate or blood, and ability to retain moisture within the wound tissue[13]. Chitosan (CS) is a natural antimicrobial material approved by the US Food and Drug Administration (FDA). It is an excellent biomaterial for the treatment of infected wounds because of its biodegradability,

excellent biocompatibility, and highly hemostatic characteristic[14]. However, CS presents poor solubility in neutral aqueous solutions, and the innate CS-based hydrogels exhibit insufficient antibacterial ability to full inhibit MRSA, which limits their potential applications to some extent [15]. Consequently, there is a need to fabricate a versatile hydrogel with excellent anti-drug-resistant bacterial effect on promoting the healing of infected skin wounds.

Zinc oxide nanoparticles (ZnO) have been investigated extensively as vehicles for drug delivery, catalysis, and antibacterial applications[16]. These nanoparticles are highly stable in physiological conditions and gradually decompose in acidic conditions. Thus, ZnO-P nanoparticles are ideal candidates for fabricating the pH-responsive drug delivery systems[17]. In addition, release of an appropriate amount of Zn^{2+} from the nanoparticles results in up-regulation of the expression of vascular endothelial growth factor (VEGF). This growth factor improves the formation of blood vessels, which is advantageous for improving wound healing[18]. Tannic acid (TA) is a biocompatible natural polyphenol derived from plants. It possesses abundant phenolic hydroxyl groups that endow the acid with strong antioxidant, antibacterial, and antiviral properties. Tannic acid is approved by the US FDA for use in humans[19]. A recent study utilized TA-europium complex for the treatment of myocardial infarction because its excellent anti-oxidative and angiogenic properties[20]. TA is a natural

antimicrobial agent that exhibits antibacterial ability through several mechanisms, including increased destabilization and permeability of the bacterial membrane, as well as destructive inactivation of the cell wall proteins and inhibition of enzyme activity[20]. In the authors' previous studies, adsorption of TA/ferric ion (TA/Fe^{3+}) and TA/gallium ion (TA/Ga^{3+}) complexes on titanium substrates produce surfaces with excellent antibacterial, anti-inflammatory, anti-oxidative, and osteogenic potential for enhancement of osseointegration[21]. One of the advantages of TA is that two or more of its phenolic hydroxyl groups can chelate with various metal ions to form a metal-phenolic network with multiple biomedical applications[22]. For example, TA/ZnO nanoparticles exhibit good antibacterial and anti-inflammatory effects for wound repair[23]. Hence, TA/ZnO nanoparticles appear to be a potential candidate for regulating immune reactions, such as M2 polarization of macrophages, in infected wounds.

It was envisaged that the desired hydrogel for the treatment of infected cutaneous wounds required the elimination of bacterial infection, alleviation of inflammatory responses in the wound site, stimulation of M2 macrophage polarization, and promotion of angiogenesis. The logistics for the synthesis of such a versatile hydrogel as wound dressing is summarized in **Scheme 1**. Phenylboronic acid-grafted chitosan (CS-PBA), dibenzaldehyde-grafted poly (ethylene glycol) (PEG-DA), phenylboronic acid-functionalized ZnO, and TA

WILEY-VCH

were used to prepare a CPP@ZnO-P-TA hydrogel *via* dynamic Schiff base reaction and

boronic ester bonds. The objectives of the present work were to examine the experimental use

of the CPP@ZnO-P-TA hydrogel as wound dressing for the treatment of MRSA-infected

cutaneous wounds, and to investigate the underlying mechanisms that expedite healing of

these wounds.

2. Results and discussion

2.1. Characterization of PBA-functionalized ZnO nanoparticles, CS-PBA and PEG-DA

The PBA-functionalized ZnO nanoparticles (ZnO-P) were uniformly distributed and had

a hexagonal crystalline structure with a diameter of ~110 nm **(Figure 1A)**. X-ray powder

diffraction of the ZnO-P nanoparticles revealed a typical hexagonal crystalline structure, with

diffraction peaks at 31.8° (100), 34.5° (002), 36.3° (101), 41.6° (102), 56.6° (110), and 61.1°

(103) (**Figure 1B**). These diffraction peaks are consistent with those exhibited by wurtzite

ZnO (Joint Committee on Powder Diffraction Standards card no. 36-1451)[24].

The CS-PBA was synthesized *via* amide reaction (**Figure S1, Supporting**

Information). Proton NMR examination of CPP (**Figure 1C**) identified four new peaks at

7.0-7.7 ppm that were ascribed to the phenyl group protons in CS-PBA. This finding is

indicative of successful modification of 3-carboxyphenylboronic acid[25]. The degree of substitution of PBA was approximately 13.2%.

The PEG-DA was obtained by esterification reaction (**Figure S2, Supporting Information**) with a yield of 85.6%. The chemical structure of PEG-DA was confirmed in the authors' previous study[14a].

2.2. Characterization of the hydrogels

The CPP@ZnO-P-TA hydrogels were sythesized using dynamic cross-linkers. The bonds formed included imide bonds between the amino groups of CS-PBA and the aldehyde groups of PEG-DA, and boronic ester bonds of cis-diols of the TA molecules binding to the multiple phenylboronic acid groups of the ZnO-P nanoparticles and CS-PBA[8, 14a]. The formation of imine linkages and boric acid esters was further proved by X-ray photoelectron spectroscopy (XPS) (**Figure S3, Supporting Information**). For CPP@ZnO-P-TA hydrogel, five characteristic peaks of Zn, O, N, C, and B were observed. The peaks of C-B (186.8 eV) and B-O (191.4 eV) were found in B1s fine spectrum, likely due to the formation of boric acid esters in the CPP@ZnO-P-TA hydrogel. The appearance of O-Zn (531.0 eV) in O 1s fine spectrum, likely due to the successful synthesis of ZnO-P nanoparticles. Furthermore, B 1s fine spectrum demonstrated that the resident B-OH (193.2 eV) was 19.1%. The C 1s fine spectrum also confirmed the existence of -C=N (286.2 eV), suggesting that the amino groups

of CS-PBA were reacted with the aldehyde groups of PEG-DA in the CPP@ZnO-P-TA hydrogel. For N 1s fine spectrum, the appearance of -N=C (399.1 eV, 49.4%), NH-C (403.3 eV, 28.0%), and -NH$_2$ (400.1 eV, 22.6%), indicating that the resident -NH$_2$ group was 22.6% in the CPP@ZnO-P-TA hydrogel. The hydrogels appeared porous, with interlinked cavities when examined by SEM after freeze-drying **(Figure 1D)**. The average pore size of the CP, CPP, and CPP@ZnO-P hydrogels was 105, 98, and 103 μm, respectively. In comparison, the CPP@ZnO-P-TA exhibited a tight structure with a smaller pore size of 75 μm. Such an observation suggests that formation of boronic ester bonds between the TA molecules and ZnO-P nanoparticles/CS-PBA improves the degree of crosslinking of the hydrogel. Previous studies reported that wound dressings with tissue adhesion properties provide a more favorable microenvironment for wound healing. Materials with multiple catechol groups are capable of adhering to wounds[26].

The CPP@ZnO-P-TA hydrogel had the strongest adhesive strength (33.6 kPa), compared with the CP (17.7 kPa), CPP (22.0 kPa), and CPP@ZnO-P hydrogels (27.4 kPa) (**Figure 1E**). These data suggest that incorporation of TA enhances the adhesion capacity of the CPP@ZnO-P-TA hydrogel, enabling it to firmly cover a wound and avoid injury by extrinsic forces. This property is beneficial for managing chronic wounds. Incorporation of TA in the CPP@ZnO-P-TA also affected the mechanical properties of the hydrogel. As

depicted in **Figure 1F**, the compressive modulus of CP and CPP hydrogels was 4.4 kPa and 4.9 kPa, respectively. Loading of PBA-functionalized ZnO (ZnO-P) nanoparticles did not remarkably affect the mechanical property of the hydrogels. The compressive modulus of CPP@ZnO-P hydrogels reached 4.6 kPa after nanoparticle loading. After the introduction of TA, the compressive modulus of CPP@ZnO-P-TA hydrogels was 6.5 kPa, which was higher than those of the other three hydrogels. This is attributed to the formation of a tight cross-linking network between the TA molecules and ZnO-P nanoparticles/CS-PBA. Rheological analysis was performed to investigate the formation of CP, CPP, CPP@ZnO-P, and CPP@ZnO-P-TA hydrogels by evaluating the shear-thinning behavior and storage moduli (G') and loss moduli (G''). As shown in **Figure S4A** (**Supporting Information**), the viscosity of CP, CPP, CPP@ZnO-P, and CPP@ZnO-P-TA hydrogels decreased with the increase of shear rate, exhibiting a typical shear-thinning behavior, which implies the hydrogel with good injectability. The cross point of G'and G" in CP, CPP, CPP@ZnO-P, and CPP@ZnO-P-TA hydrogels was approximately 86%, 90%, 136%, and 162%, respectively **(Figure S4B**, **Supporting Information**). The results indicated that the introduction of ZnO-P nanoparticles and TA increased the mechanical stability of the CPP@ZnO-P-TA hydrogel. Previous studies reported that the degradation properties of the hydrogels were affected by structural changes in the hydrogels[27]. The remaining weight (%) of degraded CPP@ZnO-P-TA hydrogels was higher than those measured for the degraded CP, CPP, and CPP@ZnO-P

hydrogels (**Figure S5, Supporting Information**). This was attributed to the formation of boronic ester bonds that delayed the degradation of the CPP@ZnO-P-TA hydrogel.

The Zn^{2+} release behavior of the CPP@ZnO-P-TA hydrogel under various conditions was investigated by inductively coupled plasma-atomic emission spectroscopy. As shown in **Figure 1G**, only a small amount of Zn^{2+} (~0.70 ppm), released from the CPP@ZnO-P-TA hydrogel, was detected in phosphate-buffered saline (PBS; pH 7.4), in the absence of H_2O_2. After 14 days, 1.26 ppm of Zn^{2+} was released from the CPP@ZnO-P-TA hydrogel in PBS, in the presence of 100 μM H_2O_2. In comparison, the amount of Zn^{2+} released from the CPP@ZnO-P-TA hydrogel after 14 days increased to 2.73 ppm after immersion in PBS (pH 5.5), in the presence of 100 μM H_2O_2. As exhibited in **Figure S6 (Supporting Information)**, a small amount of TA (22.6%) released from the CPP@ZnO-P-TA hydrogel in PBS (pH 7.4) without H2O2. After 2 days, 53.8% of the TA was released from the CPP@ZnO-P-TA hydrogel in PBS (pH 5.5) without 100 μM H2O2. However, the amount of TA released by the CPP@ZnO-P-TA hydrogel increased to 69.5% within the same incubation period of 12 h in PBS (pH 5.5) with 100 μM H2O2. The total amount of TA released from CPP@ZnO-P-TA hydrogel was 85.6 μg in PBS (pH 5.5) under 100 μM H_2O_2 conditions. The results indicate that the CPP@ZnO-P-TA hydrogel exhibit good H_2O_2-responsive and pH-responsive

properties. The results indicate that the CPP@ZnO-P-TA hydrogel exhibits good H_2O_2-responsive and pH-responsive properties.

2.3. *In vitro* antibacterial activity of the hydrogels

Recurrent bacterial infection of chronic refractory wounds occurs once the skin is punctured. Continuous exudation of plasma provides nutrients and a breeding ground for bacterial growth[28]. Hence, dressings with antibacterial properties are highly esteemed for improving the efficacy of wound healing. The antibacterial ability of the CPP@ZnO-P-TA hydrogel was investigated using MRSA, which is the most common pathogen found in suppurative wound infections. Firstly, hydrogel samples with various amounts of TA (1%, 3%, 5%, and 7%) were challenged with MRSA (**Figure S7, Supporting Information**). Compared with the control group, the viability of MRSA of CPP@ZnO-P-TA (1%), CPP@ZnO-P-TA (3%), CPP@ZnO-P-TA (5%), and CPP@ZnO-P-TA (7%), hydrogels reduced from 22.8%, 14.9%, 10.1%, 7.3%, respectively, with the increase of TA concentration. Importantly, no statistical difference was found in CPP@ZnO-P-TA (5%) and CPP@ZnO-P-TA (7%) groups. Given the above results, in the subsequent experiments, the amount of TA incorporated into the CPP@ZnO-P hydrogel was 5% and the sample was denoted as CPP@ZnO-P-TA unless otherwise stated. Next, the *in vitro* antibacterial activity of the hydrogels, including CP, CPP, CPP@ZnO-P, and CPP@ZnO-P-TA, was further

evaluated by the plate count approach[29]. Next, the *in vitro* antibacterial activity of the

hydrogels, including CP, CPP, CPP@ZnO-P, and CPP@ZnO-P-TA, was further evaluated by

the plate count approach[29]. As shown in **Figure 2A**, numerous colony-forming units (CFUs)

of MRSA were observed in the CS and CPP hydrogel groups. This observation indicates that

these two hydrogels possessed negligible antibacterial activity on MRSA. After the hydrogels

were embedded with PBA-functionalized ZnO (ZnO-P) nanoparticles, only a few CFUs

survived in the CPP@ZnO-P hydrogel, and the CPP@ZnO-P-TA hydrogel. This observation

indicates that these two hydrogels possessed potent antibacterial activity. Quantitative

analysis (**Figure 2B**) indicates that MRSA viability (%) was 103.1% in the CPP hydrogel. In

contrast, MRSA viability was reduced to 14.6% for the CPP@ZnO-P hydrogel, which was

attributed to release of Zn^{2+}. The CPP@ZnO-P-TA hydrogel exhibited the strongest

antibacterial ability; MRSA viability was merely 4.8%. These results indicate that the

antibacterial performance of CS-based hydrogels is improved by Zn^{2+} release and the

inherent antibacterial property of TA. The antibacterial property of antibiotic vancomycin

was further investigated and compared with the effects achieved using the control and

CPP@ZnO-P-TA groups. The MRSA viability of CPP@ZnO-P-TA hydrogel was 9.7%,

which was significantly lower than that of antibiotic vancomycin (18.0%) (**Figure S8A, B,**

Supporting Information). Additionally, compared with the control group, the MRSA

viability of CP hydrogel was 64.2%, indicating the insufficient antibacterial properties of CP

14

hydrogel (**Figure S9, Supporting Information**). Additionally, the CPP (Zn^{2+}), CPP-TA, CPP-TA (Zn^{2+}), and CPP@ZnO-P (TA) groups were utilized to investigate the antibacterial effect of native Zn^{2+}, as well as TA. As shown in **Figure S10** (**Supporting Information**), the MRSA viability of CPP@ZnO-P, CPP (Zn^{2+}) was significantly lower than that of CPP hydrogel. However, no statistical difference was found between the CPP@ZnO-P and CPP (Zn^{2+}) groups. Additionally, the MRSA viability of CPP-TA and CPP-TA (Zn^{2+}) was 73.4% and 6.3%, respectively. Besides, the MRSA viability of CPP and CPP-TA groups was 93.7% and 73.4%, indicating that the introduction of TA could enhance the antibacterial effect of CPP hydrogels. Meanwhile, MRSA viability was 16.7% in the CPP@ZnO-P hydrogel, however, MRSA viability was reduced to 6.6% for the CPP@ZnO-P (TA) group. Importantly, no significant difference was found between CPP@ZnO-P-TA and CPP@ZnO-P (TA) groups. It was demonstrated that the amount of released Zn^{2+} and TA could effectivity inhibit the MRSA viability.

The effect of CPP@ZnO-P-TA hydrogel on the morphology of MRSA was examined by SEM. As shown in **Figure 2C**, the MRSA membrane surface was typically spherical and smooth in the CS and CPP groups. After the MRSA were incubated with CPP@ZnO-P or CPP@ZnO-P-TA hydrogels, the MRSA membrane surface shrank and ruptured. Prior studies reported that Zn^{2+} ions alter the permeability of bacterial membranes, resulting in the

decrease in adenosine triphosphate (ATP) and leakage of cellular components (DNA/RNA).

Accordingly, alteration in bacterial membrane permeability was determined by 1-N-phenylnapthylamine (NPN) assay to reflect the integrity of the cell membrane[32]. The NPN binds to phospholipids and produces strong fluorescence once bacterial membrane permeability is altered. The relative fluorescence intensity of the CPP@ZnO-P-TA group was significantly higher than that of the CP, CPP, and CPP@ZnO-P groups (**Figure S11, Supporting Information**). As shown in **Figure 2D**, the relative ATP intensity of the CPP@ZnO-P-TA group was remarkably decreased, compared with the other three groups. Leakage of intracellular components (DNA/RNA) was measured with UV-vis spectrometry at 260 nm. After treating with the CPP@ZnO-P-TA hydrogel, the normalized DNA leakage (%) was significantly increased (**Figure 2E**). Membrane damage of MRSA was further investigated using ONPG hydrolysis. The OPNG that penetrated into bacteria reacts with intracellular β-D galactosidase to form o-nitrophenol products[31]. The intensity of ONPG hydrolysis increases upon damage of the bacterial cell membrane. Compared with the CP hydrogel, the extent of ONPG hydrolysis in CPP hydrogel was negligible (**Figure 2F**). In contrast, the extent of ONPG hydrolysis in the CPP@ZnO-P and CPP@ZnO-P-TA hydrogels were much higher than the CP and CPP hydrogels. The CPP@ZnO-P-TA hydrogels exhibited the highest extent of ONPG hydrolysis; these hydrogels induced the most severe damage to the MRSA bacterial membranes.

The potential antibacterial mechanism of the CPP@ZnO-P-TA hydrogel is illustrated in **Figure 2G**. Firstly, the multiple −NH$_2$ groups present in the CS-PBA of the CPP@ZnO-P-TA hydrogel become positively charged (-NH$_3^+$) under infected conditions. These positively-charged groups effectively interact with the negatively-charged bacterial cell membrane *via* electrostatic interaction. Secondly, pH-responsive release of Zn^{2+} and modification of TA induce damage to the MRSA cell membranes of MRSA, subsequently reducing ATP intensity and increasing the outflow of intracellular components. Thirdly, ONPG hydrolysis is significantly enhanced once the bacterial membrane is damaged, ultimately resulting in cell death.

2.4. *In vitro* cytocompatibility and ROS scavenging ability of the hydrogels

Biocompatibility is crucial for wound dressings because they are in direct contact with the blood of the wounds[32]. Consequently, a hemolytic assay was conducted to examine the hemocompatibility of the experimental hydrogels **(Figure S12, Supporting Information)**. The hemolysis ratios of CP, CPP, CPP@ZnO-P, and CPP@ZnO-P-TA hydrogels were 2.3%, 3.1%, 3.4%, and 3.2%, respectively. The results are indicative of the biocompatibility of the hydrogels.

Cytocompatibility of the hydrogels was evaluated by cytoskeletal staining. As shown in **Figure 3A**, the morphology of L929 cells was spindle-shaped in all groups. Live/dead

staining was used to investigate cell viability after 1, 3, and 5 days of culture with the hydrogel extractions. Almost all of the L929 cells were alive (green) after 3 days of incubation and dead cells (red) were rarely observed in all groups (**Figure 3B**). Lactate dehydrogenase concentration is an indicator of the cytotoxicity of biomaterials, the concentration of which is significantly elevated when the cells undergo apoptosis[33]. As shown in **Figure 3C**, the LDH concentrations in the presence of different hydrogels were similar. This indicates all the hydrogels examined exhibited no obvious toxicity to L929 cells. Similar results were achieved with the CCK-8 assay after 5 days of co-culture with L929 cells. Minimal cytotoxicity was identified in the hydrogel groups (**Figure 3D**).

Generation of excessive ROS and reactive nitrogen species (RNS) in the wound tissue creates persistent oxidative stress and a long-term inflammatory response. These events delay the wound healing process[34]. The ROS scavenging property of the CPP@ZnO-P-TA hydrogel was investigated with L929 cells in a hyper-oxidative microenvironment induced by 100 μM H_2O_2. The relative intracellular ROS intensity was detected with the ROS probe, 2, 7-dichlorodihydrofluor-escin diacetate (DCFH-DA). The L929 cells co-cultured with the CPP@ZnO-P-TA hydrogel emitted remarkably lower green fluorescence than those of CP, CPP, and CPP@ZnO-P hydrogels. This observation indicates that the CPP@ZnO-P-TA hydrogel effectively relieves intracellular oxidative stress (**Figure 3E, F**).

The RNS scavenging ability of the CPP@ZnO-P-TA hydrogel was examined using DPPH and 2,2-azino-bis(3-ethylbenzothiazoline-6-sulfonate) (ABTS) radical (ABTS$^{\bullet+}$) assay, respectively. As shown in **Figure 3G**, the CPP@ZnO-P-TA hydrogel had the highest DPPH scavenging activity (45.5%), which was significantly higher than the CP (14.9%), CPP (16.8%), or CPP@ZnO-P (15.3%) hydrogels. The ABTS$^{\bullet+}$ scavenging activity (%) exhibited a similar trend (**Figure S13, Supporting Information**). This observation confirmed that TA possessed exceptional RNS scavenging ability. This is attributed to the free catechol groups in TA that provide hydrogen atoms for the reduction of RNS[35].

Two representative ROS (O$_2^{\bullet-}$ and •OH) were employed to investigate the ROS-scavenging activities of the CPP@ZnO-P-TA hydrogel. Compared with the CP, CPP, and CPP@ZnO-P hydrogels, the CPP@ZnO-P-TA hydrogel exhibited the highest O$_2^{\bullet-}$ scavenging activity. The O$_2^{\bullet-}$ scavenging ratio (%) was 55.7% (**Figure S14, Supporting Information**). Scavenging activity is attributed to the hydrogen atom transfer effect of TA that converts O$_2^{\bullet-}$ to more stable H$_2$O$_2$[36]. The scavenging activity of ·OH was examined using a tetramethylbenzidine (TMB) probe, in which colorless TMB is oxidized to colored TMB. The CPP@ZnO-P-TA hydrogel possessed excellent ·OH scavenging activity when compared with the other three hydrogels (**Figure S15, Supporting Information**). Taken together, the

19

CPP@ZnO-P-TA hydrogel exhibited good cytocompatibility and anti-oxidative activities, and is safe to use as a wound dressing.

2.5. Immunoregulatory effect of the hydrogels

Experiments were performed to test the hypothesis that the CPP@ZnO-P-TA hydrogel alleviates inflammatory responses by inducing M1-to-M2 phase transition of macrophages. Firstly, the effect of TA on macrophage polarization was investigated by different TA concentration-contained CPP@ZnO-P-TA hydrogels, including CPP@ZnO-P-TA (1%), CPP@ZnO-P-TA (3%), CPP@ZnO-P-TA (5%), and CPP@ZnO-P-TA (7%). Compared with CPP@ZnO-P-TA (1%), CPP@ZnO-P-TA (3%), and CPP@ZnO-P-TA (7%) hydrogels, the CPP@ZnO-P-TA (5%) hydrogel remarkably down-regulated the expression of nitric oxide synthase (iNOS) (M1 phenotype markers) and up-regulated the expression of interleukin-10 (IL-10) (M2 phenotype markers) (**Figure S16A**, **Supporting Information**). The concentrations of TNF-α were significantly reduced in the CPP@ZnO-P-TA (5%) and CPP@ZnO-P-TA (7%) groups, especially in the CPP@ZnO-P-TA (5%) group. Meanwhile, the highest concentration of IL-10 was found in the CPP@ZnO-P-TA (5%) group (**Figure S16B**, **Supporting Information**)". Hence, the concentration of TA in the CPP@ZnO-P-TA hydrogel was 5% in the subsequent experiments and the sample was denoted as CPP@ZnO-P-TA. Then, the macrophage phenotype switch was investigated by immunofluorescence

staining of M1 (CD86) and M2 (CD206) macrophages. Lipopolysaccharide (LPS) was used to stimulate RAW264.7 macrophages to the pro-inflammatory M1 phenotype. Immunofluorescent staining indicated fluorescence signals of CD86 was positive in LPS-activated macrophages (M1), while the fluorescence signals of CD206 remained predominantly negative. Importantly, no obvious difference in the expression of CD86 or CD206 was found in LPS, CP, CPP, and CPP@ZnO-P groups. In comparison, the fluorescence signals of CD86 (M1 marker) were remarkably weakened in the CPP@ZnO-P-TA group, while the fluorescent signals of CD206 (M2 marker) were significantly augmented (**Figure 4A**). Flow cytometry assay was used to evaluate the expression of M2-type marker CD206. The results revealed that the expression of M2 phenotypes marker CD206 was the highest in the CPP@ZnO-P-TA group (**Figure S17**, **Supporting Information**).

Real-time polymerase chain reaction was performed to evaluate the anti-inflammatory effect of the CPP@ZnO-P-TA hydrogel on macrophage polarization. The CPP@ZnO-P-TA hydrogel significantly down-regulated the expression of interleukin-6 (IL-6) and iNOS (M1 phenotype markers). The results indicate that the CPP@ZnO-P-TA hydrogel is capable of inhibiting M1 polarization of macrophages. The expression of arginase-1 (Arg-1) and IL-10 were remarkably higher in the CPP@ZnO-P-TA hydrogel group (**Figure 4B**).

The concentrations of pro-inflammatory and anti-inflammatory cytokines of RAW264.7 cells and the bone marrow-derived macrophages (BMDMs) in each hydrogel group were quantified with ELISA. For RAW264.7 cells, The concentrations of IL-6, TNF-α, and IL-1β were significantly reduced in the CPP@ZnO-P-TA group. Conversely, the concentrations of IL-10 and TGF-β were significantly enhanced (**Figure 4C**). Especially, a similar trend was observed for the expression of TNF-α and IL-10 in the CPP@ZnO-P-TA-treated BMDMs compared with LPS, CP, CPP, and CPP@ZnO-P groups (**Figure S18**, **Supporting Information**). These results support the hypothesis that the phenol hydroxyl group of TA in the CPP@ZnO-P-TA hydrogel exerts an immunoregulatory effect by scavenging ROS and activating the transition of macrophages macrophages from the M1 to the M2 phenotype *via* the secretion of inflammatory cytokines (**Figure 4D**), thereby inhibiting the inflammatory responses. This is crucial for promoting healing of the infected wounds.

2.6. Angiogenesis of the hydrogels

Scratch assay and the transwell co-culture were used to examine the migration of L929 cells cultured with various hydrogels **(Figure 5A-D)**. Cells cultured with the CPP@ZnO-P-TA hydrogel had a higher cell migration ratio (%) than the other hydrogels after 24 h and 48 h of co-culture (**Figure 5A, C**). This may be attributed to the presence of Zn^{2+} and TA. The

aforementioned phenomenon was further confirmed by quantitative analysis of transmigrated L929 cells in the transwell co-culture system (**Figure 5B, D**).

Wound healing is an orchestrated process wherein fibroblasts synthesize matrix proteins and secrete growth factors to render the wound microenvironment conducive to repair[37]. Type I collagen (Col I) is the dominant collagen component of skin tissues, and fibronectin (FN) is an important component of the extracellular matrix (ECM). Alpha smooth muscle actin (α-SMA) and vascular endothelial growth factor (VEGF) enhance contraction and angiogenesis, respectively. Consequently, the expression of the aforementioned genes was analyzed by qRT-PCR. The CPP@ZnO-P-TA group up-regulated gene expressions of Col I, FN, α-SMA, and VEGF significantly, when compared with CP and CPP hydrogels (**Figure 5E**).

Angiogenesis is indispensable for wound repair because it supplies the wound site with oxygen and nutrition, and supports cytokine transport to the wound healing-related cells[38]. The angiogenesis potential of each hydrogel was investigated by immunofluorescence staining, ELISA, and Western blot analysis of VEGF and CD31, two commonly used makers for the evaluation of angiogenesis. Immunofluorescence staining showed that the CPP@ZnO-P and CPP@ZnO-P-TA hydrogels upregulated the expression of VEGF and CD31 in L929 cells (**Figure 5F**). The ELISA results showed that the concentrations of VEGF and CD31 were remarkably increased in the CPP@ZnO-P-TA treated group (**Figure S19, Supporting**

23

Information). Quantitative analysis of the Western blot results indicated that VEGF and CD31 expressions were the highest in the CPP@ZnO-P-TA group (**Figure 5G, H**). These results suggest that the presence of Zn^{2+} and TA significantly improve angiogenesis.

The PI3K/Akt signaling pathway improves angiogenesis by regulating cell proliferation, migration, and differentiation[6, 39]. The Akt phosphorylation levels (p-Akt) in induced pluripotent stem cells are up-regulated in the presence of Zn^{2+} and TA[6]. Hence, we speculated that enhancement of angiogenesis by the CPP@ZnO-P-TA hydrogel is accomplished *via* the PI3K/Akt signaling pathway. Accordingly, the p-Akt expression by L929 cells was analyzed with Western blot after the cells were co-cultured with different hydrogels. As shown in **Figures 5I, J**, the expressions of phosphorylated PI3K (p-PI3K) and p-Akt in the CPP@ZnO-P-TA groups were significantly higher than those in the CP, CPP, and CPP@ZnO-P groups (**Figure 5K**). These results indicate that the CPP@ZnO-P-TA hydrogel effectively stimulates the expression of angiogenic-related genes and cytokines. This is advantageous for angiogenesis and tissue remolding in the infected wound site.

2.7. *In vivo* wound healing of the hydrogels

The wound repair potential of the CPP@ZnO-P-TA hydrogel was further substantiated *in vivo* using an infected full-thickness wound model[14a]. Wound healing after treatment with different hydrogel-based dressings was monitored with macroscopic images on day 0, 3, 7, and

24

14 (**Figure 6A**). Wound areas decreased over time in all groups after 14 days (**Figure 6B**). Wounds that were covered with the CPP@ZnO-P-TA hydrogel demonstrated accelerated wound closure, whereas wounds in the other four groups were still visible on day 14.

The *in vivo* antibacterial effect of the CPP@ZnO-P-TA hydrogel was investigated by retrieving residual MRSA from the wound sites for examination using a standard plate count approach. The results revealed that the number of MSRA colonies in the CPP@ZnO-P and CPP@ZnO-P-TA groups was significantly decreased (**Figure 6C**). After quantitative analysis (**Figure 6D**), the CPP@ZnO-P-TA group had a higher antibacterial ratio against MRSA (94.7%), when compared with the CP (26.2%), CPP (27.4%), and CPP@ZnO-P (86.7%) groups. These results indicate that the CPP@ZnO-P-TA hydrogel effectively inactivates MRSA from the infected wounds, due to the synergistic antibacterial effect of ZnO-P nanoparticles and TA[40]. On day 3 and 7, wound contraction (%) in the CPP@ZnO-P and CPP@ZnO-P-TA groups were significantly higher than the other three groups (**Figure 6E**). Infected wounds that were treated with the CPP@ZnO-P-TA hydrogel had the highest wound contraction (%) on day 3 (47.8%) and day 7 (79.6%). A similar phenomenon was seen on day 14; wound contraction (%) of the control, CP, CPP, CPP@ZnO-P, and CPP@ZnO-P-TA groups was 78.8%, 85.5%, 84.1%, 89.9%, and 95.4%, respectively.

Residual bacteria in the wound sites were evaluated with Giemsa staining on day 3. As shown in **Figure 6F**, many bacteria were observed in wounds in the control, CP, and CPP groups. Conversely, only a few MRSA colonies were found in the CPP@ZnO-P group because of the potent antibacterial effect of ZnO-P nanoparticles[29]. Almost no bacteria colonies were detected in the CPP@ZnO-P-TA group. This observation suggests that the CPP@ZnO-P-TA hydrogel effectively eliminates MRSA in wound infections.

The pro-inflammatory microenvironment in infected wounds causes imbalance in immune homeostasis and over-activation of the M1-type macrophages[41]. Switching of microphages from the M1 to the M2 phenotype plays a vital role in tissue repair and regeneration[42]. Consequently, the macrophage populations in the wound tissue were evaluated with immunohistochemical and immunofluorescent staining. As shown in **Figure 6G**, M1-type macrophages (marked with CD86) were rarely observed in the wounds covered with CPP@ZnO-P-TA hydrogels, while they were extensively distributed in the other four groups. The M2 macrophages in the wound sites was marked with CD206. They predominated the wound tissues that were dressed with CPP@ZnO-P-TA hydrogel (**Figure 6H**). According to the immunofluorescent staining results, the CPP@ZnO-P-TA hydrogel had the least amount of CD86 and the highest CD206 compared with all other groups (**Figure S20**, **Supporting Information**), indicating that CPP@ZnO-P-TA hydrogel can reduce inflammatory responses.

The expression of pro-inflammatory cytokines (IL-6 and TNF-α) and anti-inflammatory cytokines (IL-10 and TGF-β) in the wounds was determined by ELISA. Infected wounds that were dressed with CPP@ZnO-P-TA hydrogel had miniscule expression of pro-inflammatory cytokines (IL-6 and TNF-α), while anti-inflammatory cytokines (IL-10 and TGF-β) were significantly increased on day 7 (**Figure S21, S22, Supporting Information**). These results indicate that the CPP@ZnO-P-TA hydrogel alleviates inflammatory response by inducing the transformation of macrophage from the pro-inflammatory to the anti-inflammatory phenotype. Reprogramming of the microenvironment *via* immunoregulation is beneficial for healing of infected wounds.

The regenerated skin tissues were stained with hematoxylin-eosin (H&E), Masson's trichrome, and immunohistochemical stains. In images stained with H&E (**Figure 7A, Figure S23**), a large number of inflammatory cells accumulated in the control group 3 days after treatment. In comparison, a relatively mild inflammatory infiltrate was identified in wound tissues that were treated with the CPP@ZnO-P-TA hydrogel. Quantitative analysis of the day 7 results indicated that the number of hair follicles in the CPP@ZnO-P-TA group was remarkably greater than that in other groups (**Figure 7B**). After treatment for 14 days, wounds in the control group demonstrated delayed healing and re-epithelialization, with absence of hair follicles and disorganized collagen bundles. Conversely, wounds treated with the CPP@ZnO-

27

P-TA hydrogel were completely re-epithelialized, and exhibited organized skin layer structure, with dense and orderly-arranged collagen depositions (**Figure 7A**). Collagen deposition in the control, CP, CPP, CPP@ZnO-P, and CPP@ZnO-P-TA groups was 24.0%, 22.8%, 29.7%, 42.9%, and 60.6%, respectively (**Figure 7C**). These results indicate that the CPP@ZnO-P-TA hydrogel promotes repair of infected wounds by suppressing the inflammatory response, improving wound contraction, promoting hair follicle regeneration, and collagen deposition.

Previous studies reported that angiogenesis that occurs after resolution of inflammation promotes fibroblast migration and proliferation, collagen deposition, and re-epithelialization *via* the delivery of growth factors and nutrients to the wound sites[43]. Immunohistochemical staining of VEGF and CD31 was employed to examine the formation of new blood vessels in the wound sites. As shown in **Figure 7A**, less VEGF expression was found in the control, CP, and CPP groups. The highest VEGF expression was observed in the CPP@ZnO-P-TA group. Likewise, intense CD31 staining and well-formed blood vessels were observed in the CPP@ZnO-P-TA group, with a density of 91.7 blood vessels/mm^2 (**Figure 7D**). Immunofluorescent staining results indicated that the wounds treated with CPP@ZnO-P-TA hydrogel presented significantly higher level of CD31 on day 7 than the control, CP, CPP, and CPP@ZnO-P groups. Besides, the expression of CD31 in the CPP@ZnO-P group was remarkably higher than those in the control, CP, and CPP groups (**Figure S24, Supporting**

Information). Similar trends were identified when the expression of VEGF and CD31 was investigated with ELISA (**Figure S25, Supporting Information**). These results prove that the release of Zn^{2+} and TA has advantages in promoting angiogenesis and accelerating wound healing.

Biosafety of various hydrogels *in vivo* was evaluated with whole blood biochemical analysis[44, 45]. There were no statistically significant differences among the experimental groups for white blood cells, neutrophils, red blood cells, hemoglobin, hematocrit, and platelet counts (**Figure S26, Supporting Information**). These results highlight that the CPP@ZnO-P-TA hydrogel has potential for MRSA-infected cutaneous wound management

3. Conclusion

In summary, a versatile hydrogel dressing (CPP@ZnO-P-TA) was synthesized to facilitate wound healing and skin tissue repair in an MRSA-infected cutaneous wound model. The biocompatible CPP@ZnO-P-TA hydrogel was similar to the ECM and possessed antibacterial and anti-oxidant properties, pH-responsive capacities, and the ability to restore intracellular redox homeostasis. This versatile hydrogel also stimulated polarization of macrophages to the M2 phenotype to relieve inflammation *via* the PI3K/Akt pathway, and improved VEGF-mediated neovascularization. This all-in-one hydrogel appears to have the

ability to reprogram the inflammatory microenvironment to expedite healing of MRSA-infected cutaneous wounds.
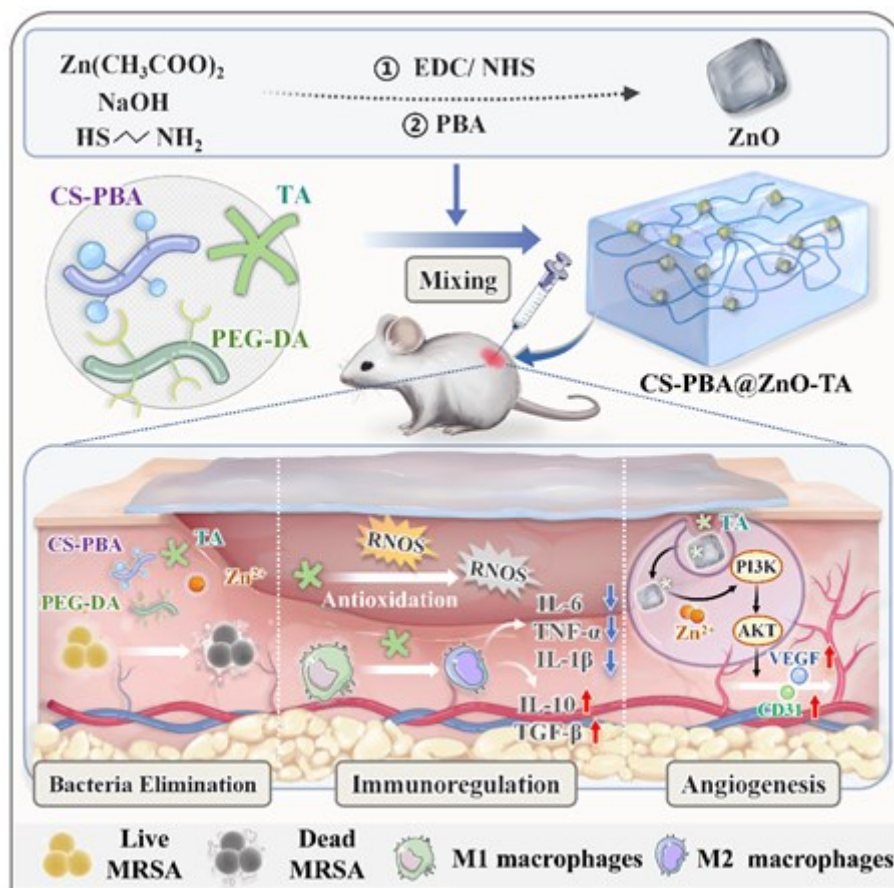
Scheme 1. Schematic diagram of the MRSA-infected wound healing promotion by the CPP@ZnO-P-TA hydrogel.

WILEY-VCH
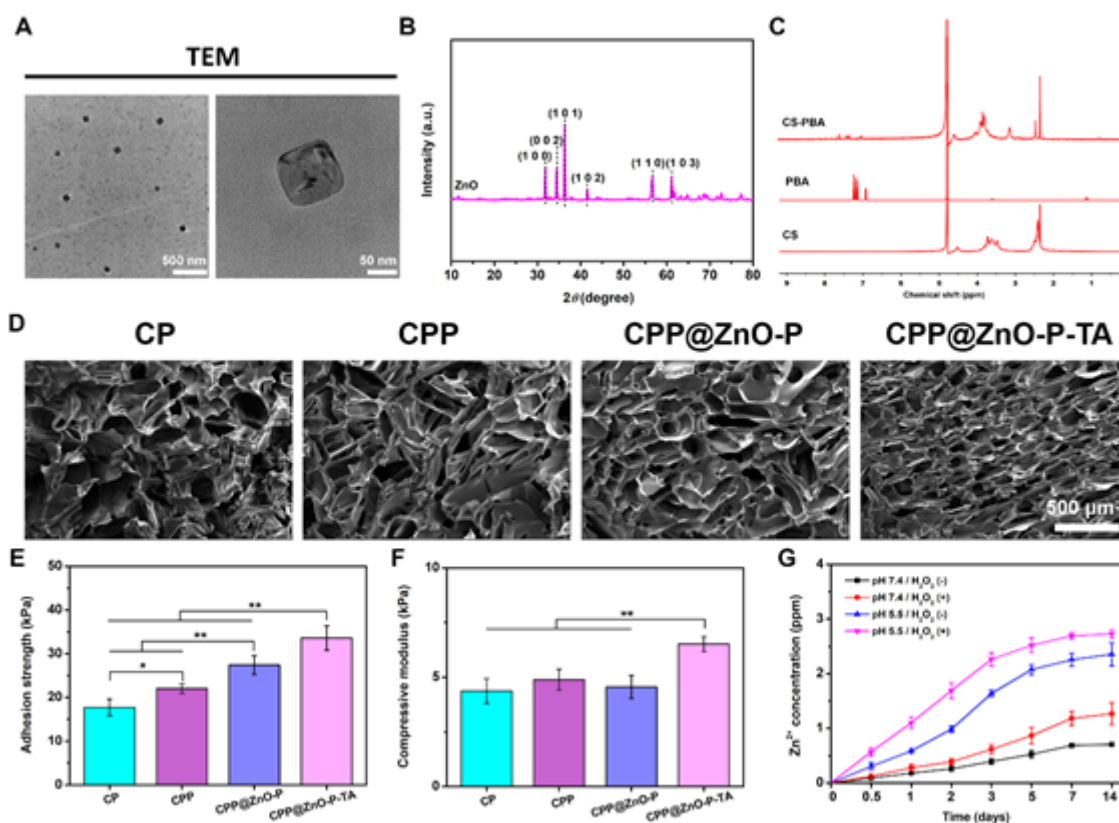
Figure 1. Characterization of the hydrogels. (A) TEM image and (B) XRD spectra of the ZnO-P nanoparticles. (C) ^{1}H NMR spectra of CP, PBA, and CPP. (D) SEM images of CP, CPP, CPP@ZnO-P, and CPP@ZnO-P-TA hydrogels. (D) Adhesion strengths and (E) compressive modulus of various hydrogels. (G) Release profiles of Zn^{2+} from the CPP@ZnO-P-TA hydrogel under different conditions for 14 days.
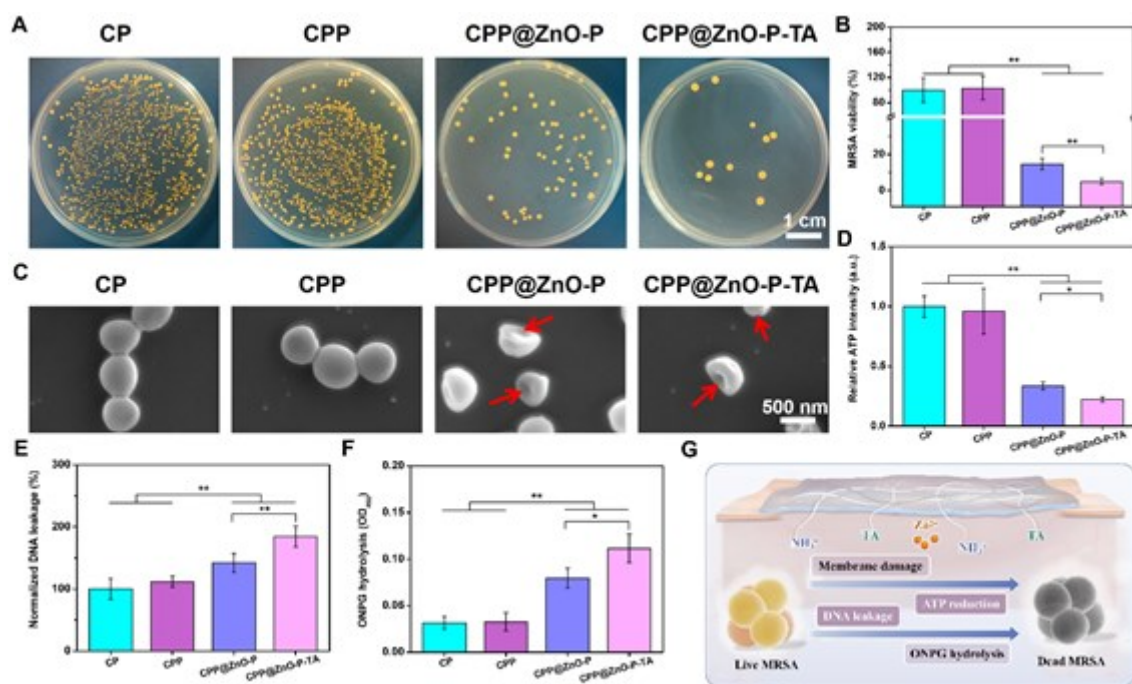
Figure 2. The antibacterial property of the hydrogels. (A) Representative photographs of bacterial colonies on LB plates after exposure to CP, CPP, CPP@ZnO-P, and CPP@ZnO-P-TA hydrogels (200 µL) for 24 h. (B) Statistical analysis of the relative viability of MRSA according to the plate counting method. (C) Morphology of bacteria after different treatments for 6 h, the red arrows indicate the damaged morphology of MRSA. (D) Relative ATP intensity, (E) normalized DNA leakage, and (F) ONPG hydrolysis of MRSA after incubation with CP, CPP, CPP@ZnO-P, and CPP@ZnO-P-TA hydrogels (200 µL) (n = 3), *$p < 0.05$, **$p < 0.01$. (G) Potential antibacterial mechanism of the CPP@ZnO-P-TA hydrogel.
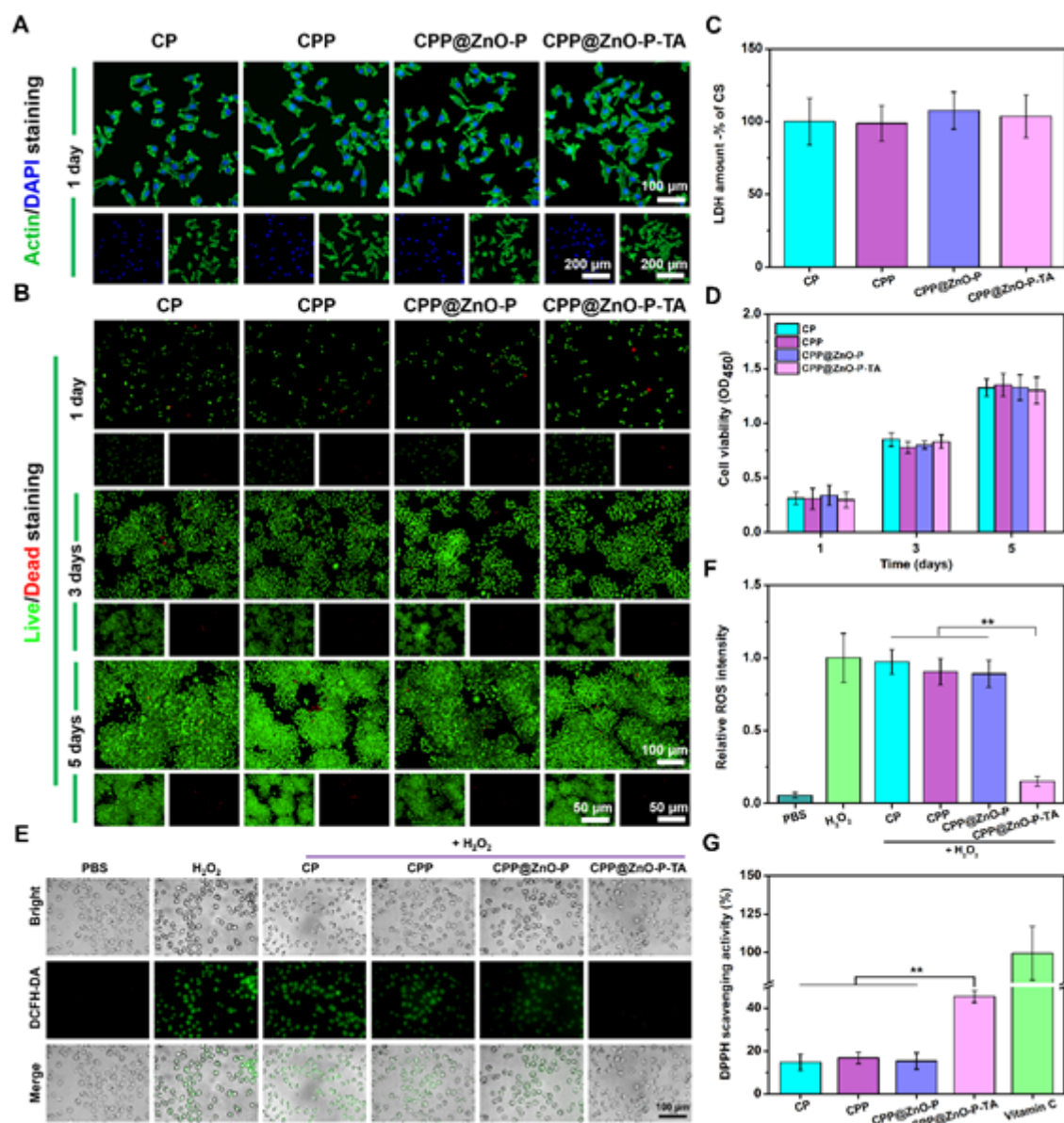
Figure 3. Biocompatibility and antioxidation of the hydrogels. (A) CLSM images of the cytoskeleton of L929 cells after exposure to various hydrogels (100 µL) for 1 day. (B) Fluorescence images of FDA/PI-stained L929 cells of the hydrogels (200 µL). (C) LDH and (D) CCK-8 assays of the hydrogels (100 µL) for 1, 3, and 5 days. (E) Representative photographs of intracellular ROS of each hydrogels (200 µL) were investigated by the ROS indicator DCFH-DA (10 µM) for 30 min. (F) Quantitative results of fluorescent intensity of

33

intracellular ROS generation in L929 cells. (G) DPPH scavenging activity of the hydrogels (200 µL) (n = 3), *$p < 0.05$, **$p < 0.01$.
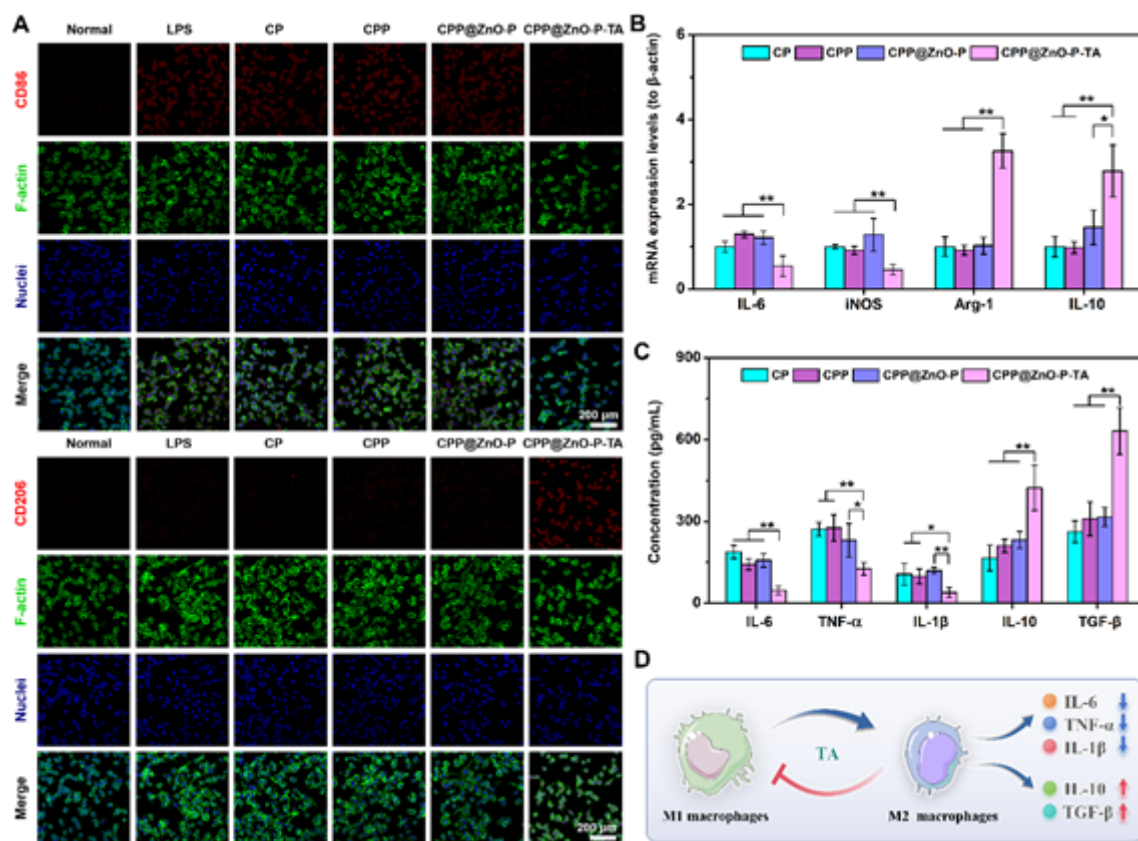

Figure 4. Immunoregulatory and anti-inflammatory properties of the hydrogels. (A) Representative immunofluorescence staining images of CD86 and CD206 after treating with various hydrogel (200 µL) for 2 days. (B) mRNA levels of inflammation-related genes IL-6, iNOS, Arg-1, and IL-10 for 2 days. (C) ELISA results of inflammatory (IL-6, TNF-α, and IL-1β) and anti-inflammatory cytokines (IL-10 and TGF-β) of RAW264.7 cells (n = 3) for 2 days, *$p < 0.05$, **$p < 0.01$. (D) Schematic diagram of the immunoregulatory and anti-inflammatory capacities of the CPP@ZnO-P-TA hydrogel.
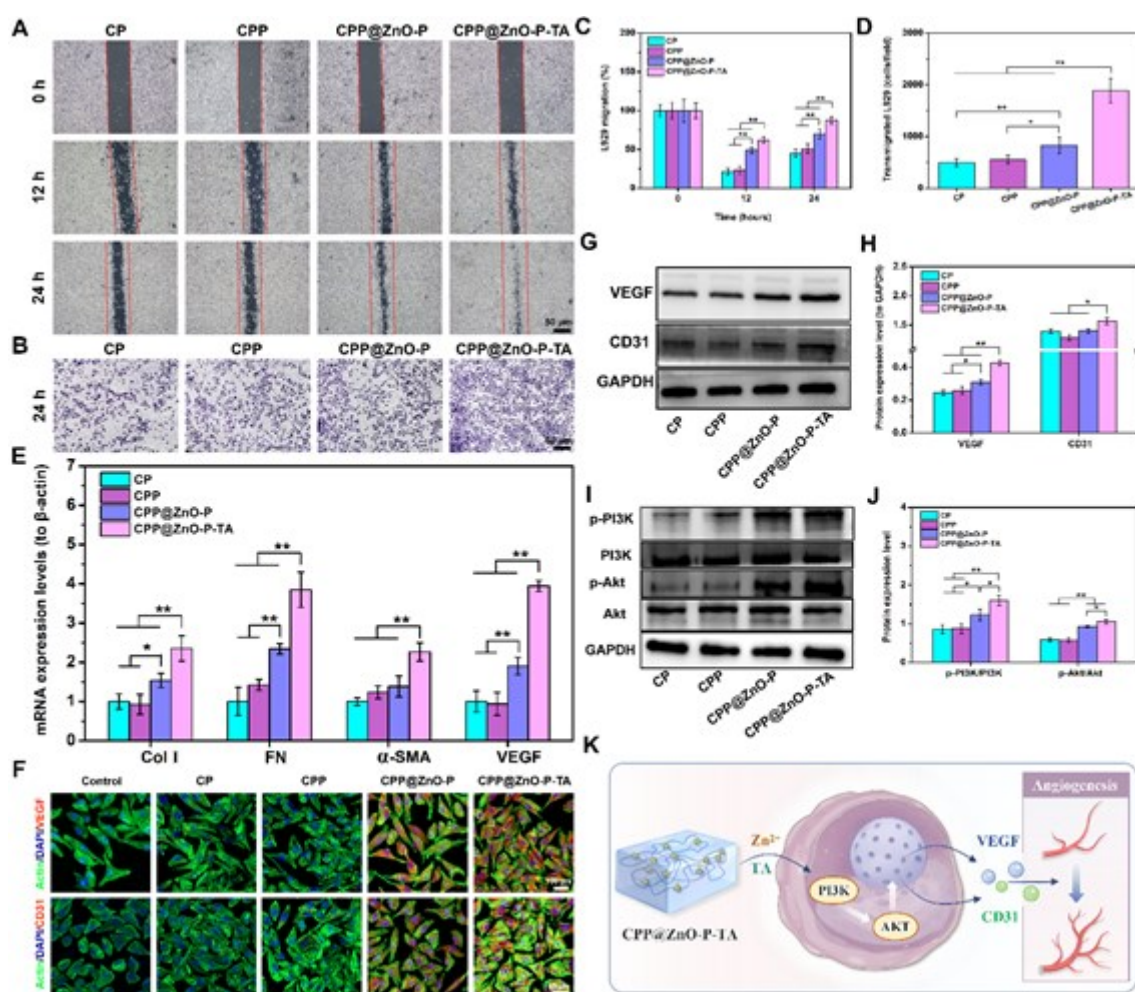
Figure 5. *In vitro* angiogenic capacity of the hydrogels. (A) Representative images of wound healing. (B) L929 cell migration of various hydrogel (200 µL) by transwell co-culture system for 24 h. (C) L929 cell scratch healing ratios after various treatments for 12 and 24 h, respectively. (D) Quantitative results of transmigrated L929 cells. (E) mRNA levels of wound healing-related genes Col I, FN, α-SMA, and VEGF with various hydrogel (200 µL) for 2 days. (F) Immunofluorescence staining images of VEGF and CD31 in various groups for 2 days. (G, H) The protein expressions of VEGF and CD31 of each hydrogel were investigated by western blot. (I, J) The expression of p-PI3K and p-Akt in each group was measured by western blot (n = 3), *$p < 0.05$, **$p < 0.01$. (K) Schematic diagram of the angiogenic capacity of the CPP@ZnO-P-TA hydrogel.

35
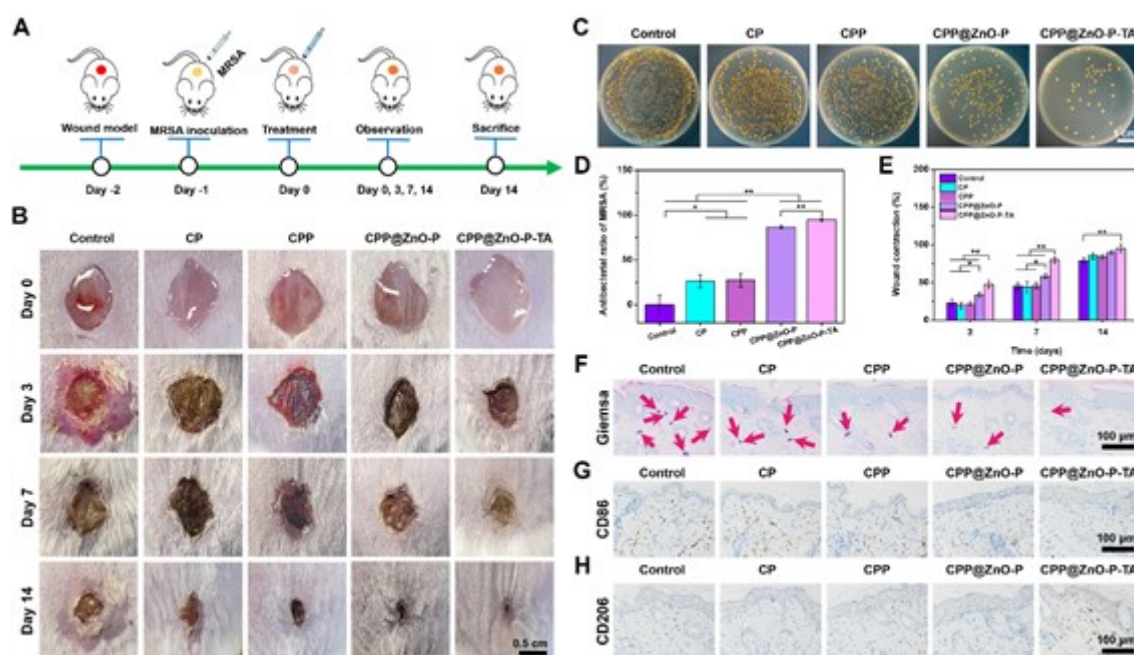
Figure 6. *In vivo* antibacterial and anti-inflammatory capacities of the hydrogels. (A) Schematic diagram of the establishment of the MRSA-infected wounds animal model and treatment timeline. (B) Photographs of the healing process of wounds in various groups. (C) Representative images of MRSA clones on LB plates stripped from the infected wound sites. (D) Quantitative results of the antibacterial ratios of MRSA treated with PBS (control), CP, CPP, CPP@ZnO-P, and CPP@ZnO-P-TA hydrogels (100 μL) on day 3. (E) Wound contraction (%) during the healing process (n = 3), *$p < 0.05$, **$p < 0.01$. (F) Giemsa staining of wound tissues (red arrow: residual bacteria) on day 3. (G, H) Immunohistochemistry staining images of CD86 and CD206 of the regenerated wounds in each group.
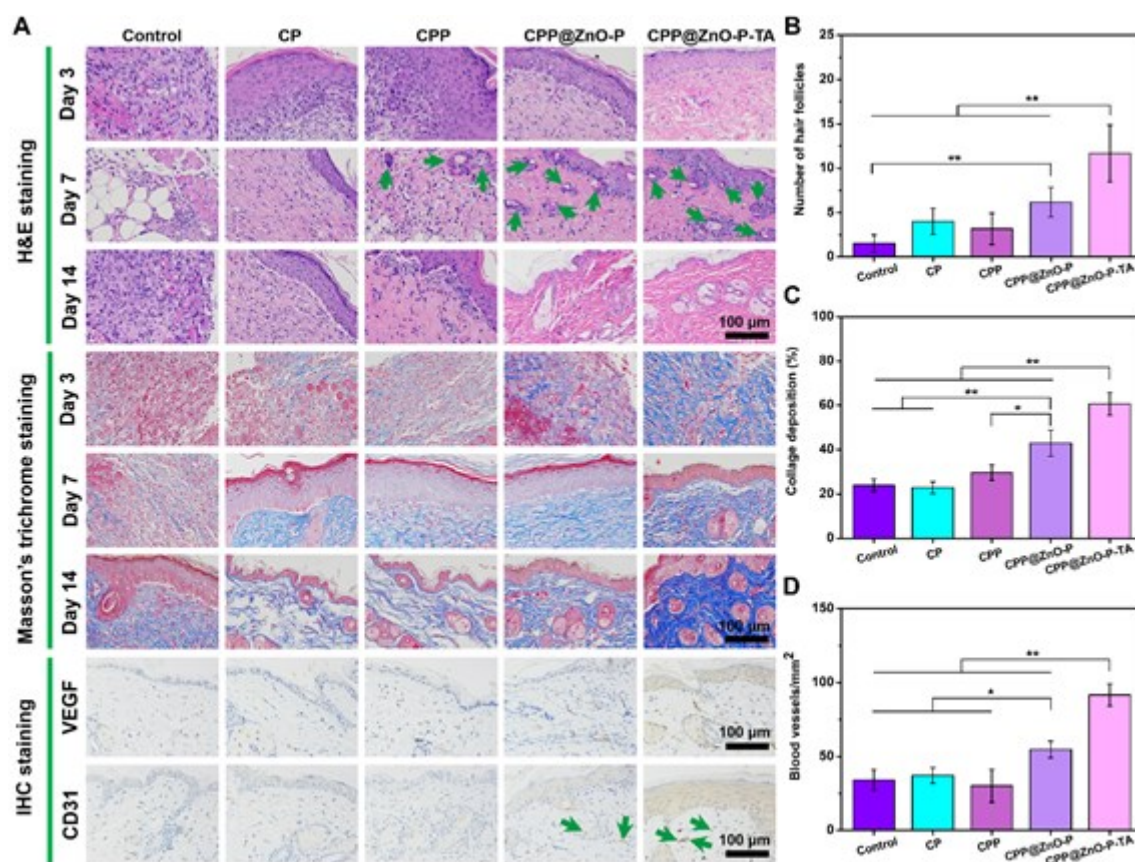
Figure 7. *In vivo* wound healing efficacy of the hydrogels. (A) H&E, Masson's trichrome, and immunohistochemistry staining of regenerated skin treated with PBS (control), CP, CPP, CPP@ZnO-P, and CPP@ZnO-P-TA hydrogels (100 μL). Blue arrows and black squares indicate the hair follicle and collagen deposition in the H&E and Masson's trichrome staining, respectively. Blue arrows suggest the neovascularization of CD31-immunohistochemistry staining. (B-D) Quantitative analysis of the number of hair follicles, the ratios of collagen deposition, and the intensity of blood vessels, respectively (n = 3), $*p < 0.05$, $**p < 0.01$.

Conflict of Interest

The authors declare no conflict of interest.

Supporting Information

Supporting Information is available from the Wiley Online Library or from the author.

WILEY-VCH

Acknowledgements

References:

[1] a) Y. Liang, Y. Liang, H. Zhang, B. Guo, *Asian J. Pharm. Sci.* **2022**, 17, 353; b) M. Xu, X. Su, X. Xiao, H. Yu, X. Li, A. Keating, S. Wang, R. C. Zhao, *Aging Dis.* **2021**, 12, 102.

[2] a) L. Qiao, Y. Liang, J. Chen, Y. Huang, S. A. Alsareii, A. M. Alamri, F. A. Harraz, B. Guo, *Bioact. Mater.* **2023**, 30, 129; b) X. Yu, J. Zhao, X. Ma, D. Fan, *Chem. Eng. J.* **2023**, 465, 142933.

[3] a) Y. Jiao, F. R. Tay, L.-n. Niu, J.-h. Chen, *Int. J. Oral Sci.* **2019**, 11, 28; b) Y. Jiao, L.-N. Niu, S. Ma, J. Li, F. R. Tay, J.-h. Chen, *Prog. Polym. Sci.* **2017**, 71, 53; c) J. Wu, P. Shen, X.

38

WILEY-VCH

Qin, Y. Yang, C. Lin, X. Li, W. Geng, P. Gao, L. Chen, L. Miao, *Chem. Eng. J.* **2023**, 459, 141507.

[4] a) W. Zhang, K. Zha, Y. Xiong, W. Hu, L. Chen, Z. Lin, C. Yu, W. Zhou, F. Cao, H. Hu, *Bioact. Mater.* **2023**, 30, 29; b) H. Cho, M. R. Blatchley, E. J. Duh, S. Gerecht, *Adv. Drug Delivery Rev.* **2019**, 146, 267.

[5] a) K. Zha, Y. Xiong, W. Zhang, M. Tan, W. Hu, Z. Lin, P. Cheng, L. Lu, K. Cai, B. Mi, *ACS Nano* **2023**, 17, 17199; b) S. Wang, H. Zheng, L. Zhou, F. Cheng, Z. Liu, H. Zhang, Q. Zhang, *Biomaterials* **2020**, 260, 120314; c) S. Wang, H. Zheng, L. Zhou, F. Cheng, Z. Liu, H. Zhang, L. Wang, Q. Zhang, *Nano Lett.* **2020**, 20, 5149.

[6] Y. Wu, Y. Wang, C. Zheng, C. Hu, L. Yang, Q. Kong, H. Zhang, Y. Wang, *Adv. Funct. Mater.* **2023**, 2305992.

[7] a) H. Zhao, J. Huang, Y. Li, X. Lv, H. Zhou, H. Wang, Y. Xu, C. Wang, J. Wang, Z. Liu, *Biomaterials* **2020**, 258, 120286; b) L. Siebert, E. Luna-Cerón, L. E. García-Rivera, J. Oh, J. Jang, Y. K. Mishra, D. A. Rosas-Gómez, M. D. Pérez-Gómez, G. Maschkowitz, H. Fickenscher, *Adv. Funct. Mater.* **2021**, 31, 2007555.

[8] C. Årdal, M. Balasegaram, R. Laxminarayan, D. McAdams, K. Outterson, J. H. Rex, N. Sumpradit, *Nat. Rev. Microbiol.* **2020**, 18, 267.

[9] Y. Xiong, B.-B. Mi, Z. Lin, Y.-Q. Hu, L. Yu, K.-K. Zha, A. C. Panayi, T. Yu, L. Chen, Z.-P. Liu, *Mil. Med. Res.* **2022**, 9, 65.

[10] M.-L. Luo, Y. Jiao, W.-p. Gong, Y. Li, L.-N. Niu, F. R. Tay, J.-h. Chen, *J. Dent.* **2020**, 94, 103297.

[11] J. Ye, C. Xie, C. Wang, J. Huang, Z. Yin, B. C. Heng, X. Chen, W. Shen, *Bioact. Mater.* **2021**, 6, 4096.

[12] a) Y. Liang, Z. Li, Y. Huang, R. Yu, B. Guo, *ACS Nano* **2021**, 15, 7078; b) E. Jirigala, B. Yao, Z. Li, Y.-J. Zhang, C. Zhang, L.-T. Liang, F.-L. Zhang, X.-Y. Yuan, X.-L. Duan, W. Song, *Mil. Med. Res.* **2023**, 10, 17; c) X. Chen, X. Li, W. He, M. Wang, A. Gao, L. Tong, S. Guo, H. Wang, G. Pan, *Innovation* **2023**, 4, 100483.

[13] Y. Liang, J. He, B. Guo, *ACS Nano* **2021**, 15, 12687.

[14] a) B. Tao, C. Lin, Z. Yuan, Y. He, M. Chen, K. Li, J. Hu, Y. Yang, Z. Xia, K. Cai, *Chem. Eng. J.* **2021**, 403, 126182; b) M. M. Islam, M. Shahruzzaman, S. Biswas, M. N. Sakib, T. U. Rashid, *Bioact. Mater.* **2020**, 5, 164.

[15] a) W. Wang, C. Xue, X. Mao, *Int. J. Biol. Macromol.* **2020**, 164, 4532; b) Y. Yu, C. Wang, Q. Fu, Y. Wan, Carbohyd. Polym. **2024**, 327, 121635. c) Y. Jin, C. Wang, Z. Xia, P. Niu, Y. Li, W. Miao, Carbohyd. Polym. 2023, 306, 1205689.

WILEY-VCH

[16] J. Ma, C. Wu, *Exploration* **2022**, 2, 20210083.

[17] J. Li, L. Tan, X. Liu, Z. Cui, X. Yang, K. W. K. Yeung, P. K. Chu, S. Wu, *ACS Nano* **2017**, 11, 11250.

[18] Y. Ju, H. Zeng, X. Ye, M. Dai, B. Fang, L. Liu, *Mater. Today Bio* **2023**, 22, 100739.

[19] L. Yang, L. Han, L. Jia, *ACS Appl. Mater. Interfaces* **2016**, 8, 26570.

[20] a) K. Wu, W. Hua, X. Li, J. Lin, *Chem. Eng. J.* **2022**, 446, 136835. b) Z. Ahmadian, A. Correia, M. Hasany, P. Figueiredo, F. Dobakhti, M.R. Eskandari, S.H. Hosseini, R. Abiri, S. Khorshid, J. Hirvonen, H.A. Santos, M-A. Shahbazi, *Adv. Healthcare Mater.* **2023**, 2001122.

[21] a) K. Xu, C. Mu, C. Zhang, S. Deng, S. Lin, L. Zheng, W. Chen, Q. Zhang, *Biomaterials* **2023**, 301, 122268; b) Y. Ding, G. Liu, S. Liu, X. Li, K. Xu, P. Liu, K. Cai, *Adv. Healthcare Mater.* **2023**, 2300722.

[22] a) M. A. Rahim, S. L. Kristufek, S. Pan, J. J. Richardson, F. Caruso, *Angew. Chem. Int. Ed.* **2019**, 58, 1904; b) G. Yun, Q. A. Besford, S. T. Johnston, J. J. Richardson, S. Pan, M. Biviano, F. Caruso, *Chem. Mater.* **2018**, 30, 5750.

[23] Y. Yang, B. Tao, Y. Gong, R. Chen, W. Yang, C. Lin, M. Chen, L. Qin, Y. Jia, K. Cai, *J. Biomed. Mater. Res. Part A* **2020**, 108, 2190.

[24] a) L. Wang, S. Liu, X. Feng, Q. Xu, S. Bai, L. Zhu, L. Chen, Y. Qin, Z. L. Wang, *ACS Nano* **2017**, 11, 4859; b) A. Phuruangrat, P. Dumrongrojthanath, O. Yayapao, J. Arin, S. Thongtem, T. Thongtem, *Rare Met.* **2016**, 35, 390.

[25] X. Li, K. Xu, Y. He, B. Tao, K. Li, C. Lin, J. Hu, J. Wu, Y. Wu, S. Liu, *Biomaterials* **2022**, 287, 121683.

[26] a) H. Chen, Y. Cheng, J. Tian, P. Yang, X. Zhang, Y. Chen, Y. Hu, J. Wu, *Sci. Adv.* **2020**, 6, eaba4311; b) X. Han, S. Chen, Z. Cai, Y. Zhu, W. Yi, M. Guan, B. Liao, Y. Zhang, J. Shen, W. Cui, *Adv. Funct. Mater.* **2023**, 33, 2213008.

[27] B. Tao, C. Lin, X. Qin, Y. Yu, A. Guo, K. Li, H. Tian, W. Yi, D. Lei, Y. Chen, *Mater. Today Bio* **2022**, 13, 100216.

[28] a) Z. Yuan, J. Wu, Y. Xiao, H. Yang, S. Meng, L. Dai, P. Li, K. Cai, *Adv. Funct. Mater.* **2023**, 2302908; b) G. C. Gurtner, S. Werner, Y. Barrandon, M. T. Longaker, *Nature* **2008**, 453, 314.

[29] X. Wang, Q. Shi, Z. Zha, D. Zhu, L. Zheng, L. Shi, X. Wei, L. Lian, K. Wu, L. Cheng, *Bioact. Mater.* **2021**, 6, 4389.

[30] B. Tao, W. Yi, X. Qin, J. Wu, K. Li, A. Guo, J. Hao, L. Chen, *J. Mate. Sci. Technol.* **2023**, 146, 131.

WILEY-VCH

[31] Z. Zhang, Y. Wang, W. Teng, X. Zhou, Y. Ye, H. Zhou, H. Sun, F. Wang, A. Liu, P. Lin, *Biomaterials* **2021**, 274, 120853.

[32] R. Wang, J. Li, W. Chen, T. Xu, S. Yun, Z. Xu, Z. Xu, T. Sato, B. Chi, H. Xu, *Adv. Funct. Mater.* **2017**, 27, 1604894.

[33] a) B. Zou, Z. Xiong, L. He, T. Chen, *Biomaterials* **2022**, 285, 121549; b) M. Zaborowska, F. Vazirisani, F. A. Shah, R. Firdaus, O. Omar, K. Ekström, M. Trobos, P. Thomsen, *Biomaterials* **2021**, 278, 121158.

[34] S. Hu, Z. Yang, Q. Zhai, D. Li, X. Zhu, Q. He, L. Li, R. D. Cannon, H. Wang, H. Tang, *Small* **2023**, 2207437.

[35] Y. Li, L. Yang, Y. Hou, Z. Zhang, M. Chen, M. Wang, J. Liu, J. Wang, Z. Zhao, C. Xie, *Bioact. Mater.* **2022**, 18, 213.

[36] Y. Xu, Y. Luo, Z. Weng, H. Xu, W. Zhang, Q. Li, H. Liu, L. Liu, Y. Wang, X. Liu, *ACS Nano* **2023**, 17, 18732.

[37] Y. He, K. Li, X. Yang, J. Leng, K. Xu, Z. Yuan, C. Lin, B. Tao, X. Li, J. Hu, *Small* **2021**, 17, 2102907.

[38] L. Yang, F. Liang, X. Zhang, Y. Jiang, F. Duan, L. Li, F. Ren, *Chem. Eng. J.* **2022**, 427, 131506.

[39] Y. Wang, D. Yin, C. Xu, K. Wang, L. Zheng, Y. Zhang, *Cell Biosci.* **2016**, 6, 1.

[40] A. Farazin, M. Mohammadimehr, H. Naeimi, *Int. J. Biol. Macromol.* **2023**, 241, 124572.

[41] a) Z. Yuan, C. Lin, L. Dai, Y. He, J. Hu, K. Xu, B. Tao, P. Liu, K. Cai, *Small* **2021**, 17, 2007522; b) L. Tan, M. Li, H. Chen, Y. Zhang, Y. Liu, M. Chen, Z. Luo, K. Cai, Y. Hu, *Nano Today* **2023**, 52, 101962.

[42] [42] B.-J. Zhang, M. Zhang, Y.-H. Sun, M.-M. Li, F. Han, C.-T. Wu, *Prog. Nat. Sci.* **2021**, 31, 883–890.

[43] a) Z. Liang, W. Liu, Z. Wang, P. Zheng, W. Liu, J. Zhao, Y. Zhong, Y. Zhang, J. Lin, W. Xue, *Acta Biomater.* **2022**, 143, 428; b) S. C. Funes, A. M. de Lara, M. J. Altamirano-Lagos, J. P. Mackern-Oberti, J. Escobar-Vera, A. M. Kalergis, *Autoimmun. Rev.* **2019**, 18, 359.

[44] Y.-L. Yu, J.-J. Wu, C.-C. Lin, X. Qin, F. R. Tay, L. Miao, B.-L. Tao, Y. Jiao, *Mil. Med. Res.* **2023**, 10, 21.

WILEY-VCH

[45] B. Tao, H. Lan, X. Zhou, C. Lin, X. Qin, M. Wu, Y. Zhang, S. Chen, A. Guo, K. Li,
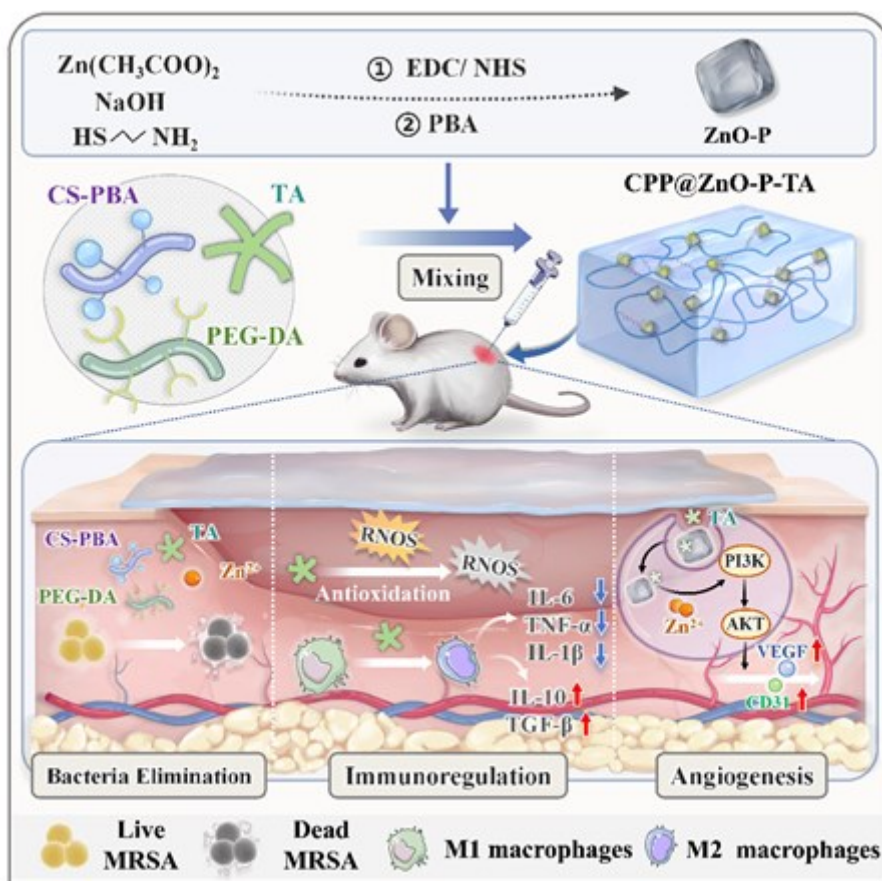
Mater. Des. **2023**, 233, 112268.

The table of contents entry:

The ZnO-P nanoparticle emblebbed composite hydrogel is fabricated based on Schiff base and borate ester cross-linked reaction. The CPP@ZnO-P-TA hydrogel presents pH-responsive release of Zn^{2+} and TA, which is beneficial for killing MRSA. Meanwhile, this hydrogel alleviates oxidative stress, stimulates M2 polarization of macrophages, and induces neovascularization *via* the PI3K/Akt pathway. Furthermore, the hydrogel could significantly promote MRSA-infected cutaneous wounds healing by improving antibacterial ability, alleviating inflammatory responses, stimulating angiogenesis, and facilitating collagen deposition.

WILEY-VCH

Ye Zhang, Sinan Chen, Xian Qin, Ai Guo, Kai Li, Lixue Chen, Weiwei Yi, Zhongliang Deng, Franklin R. Tay, Wenbo Geng[*], Li Miao[*], Yang Jiao[*], Bailong Tao[*]

A Versatile Chitosan-based Hydrogel Accelerates Infected Wound Healing *via* Bacterial Elimination, Antioxidation, Immunoregulation, and Angiogenesis